

# The GAPS programme at TNG<sup>★</sup>

## LXXI. HD 128717 B/Gaia-6 B: a long-period eccentric low-mass brown dwarf from astrometry and radial velocities

M. Pinamonti<sup>1</sup>, A. Sozzetti<sup>1</sup>, D. Barbato<sup>2</sup>, S. Desidera<sup>2</sup>, K. Biazzo<sup>3</sup>, A. S. Bonomo<sup>1</sup>, A. F. Lanza<sup>4</sup>, L. Naponiello<sup>1</sup>, L. Affer<sup>5</sup>, R. M. Anche<sup>6</sup>, G. Andreuzzi<sup>7,3</sup>, M. Basilicata<sup>1</sup>, M. Brinjkij<sup>8</sup>, M. Brogi<sup>1,9</sup>, L. Cabona<sup>10</sup>, E. Carolo<sup>2</sup>, S. Colombo<sup>5</sup>, M. Damasso<sup>1</sup>, M. D'Arpa<sup>5</sup>, S. Di Filippo<sup>2</sup>, A. Harutyunyan<sup>7</sup>, J. Hom<sup>6</sup>, L. Mancini<sup>11,1,12</sup>, G. Mantovan<sup>14,2</sup>, D. Nardiello<sup>13,2,14</sup>, K. K. R. Santhakumari<sup>2</sup>, and T. Zingales<sup>13,2</sup>

<sup>1</sup> INAF - Osservatorio Astrofisico di Torino, Via Osservatorio 20, I-10025 Pino Torinese, Italy  
e-mail: [matteo.pinamonti@inaf.it](mailto:matteo.pinamonti@inaf.it)

<sup>2</sup> INAF - Osservatorio Astronomico di Padova, vicolo dell'Osservatorio 5, I-35122 Padova, Italy

<sup>3</sup> INAF - Osservatorio Astronomico di Roma, Via Frascati 33, I-00078 Monte Porzio Catone, Italy

<sup>4</sup> INAF - Osservatorio Astrofisico di Catania, Via S. Sofia 78, I-95123 Catania, Italy

<sup>5</sup> INAF - Osservatorio Astronomico di Palermo, piazza del Parlamento 1, I-90134 Palermo, Italy

<sup>6</sup> Department of Astronomy and Steward Observatory, The University of Arizona, 933 North Cherry Ave, Tucson, AZ85721, USA

<sup>7</sup> Fundación Galileo Galilei - INAF, Ramble José Ana Fernandez Pérez 7, E-38712 Breña Baja, TF, Spain

<sup>8</sup> School of Earth and Space Exploration, Arizona State University, 781 E Terrace Mall, Tempe, AZ 85287, USA

<sup>9</sup> Department of Physics, University of Turin, Via Pietro Giuria 1, 10125 Torino, Italy

<sup>10</sup> INAF - Osservatorio Astronomico di Brera, Via E. Bianchi 46, I-23807 Merate, Italy

<sup>11</sup> Dipartimento di Fisica, Università di Roma "Tor Vergata", Via della Ricerca Scientifica 1, I-00133 Roma, Italy

<sup>12</sup> Max Planck Institute for Astronomy, Königstuhl 17, DE-69117 Heidelberg, Germany

<sup>13</sup> Dipartimento di Fisica e Astronomia, Università degli Studi di Padova, Vicolo dell'Osservatorio 3, 35122 Padova, Italy

<sup>14</sup> Centro di Ateneo di Studi e Attività Spaziali "G. Colombo" – Università degli Studi di Padova, Via Venezia 15, 35131 Padova, Italy

<sup>15</sup> INAF - Osservatorio Astronomico di Brera, Via E. Bianchi 46, I-23807 Merate, Italy

### ABSTRACT

**Context.** The transition regime between giant planets (GPs) and brown dwarfs (BDs) is still an open subject of study in exoplanetary science. A complete understanding of the population of long-period GPs and BDs would be pivotal in understanding this topic, but the number of such objects with precisely measured orbital and physical parameters is still small. Moreover, their dynamical influence on smaller companions in inner orbits is still unclear.

**Aims.** Within the GAPS programme, we aim to confirm and characterize sub-stellar companion candidates from Gaia DR3, and to study the potential presence of additional lower-mass planets in their systems.

**Methods.** We present the results of an intensive high-precision radial velocity (RV) monitoring of HD 128717, which hosts the astrometric candidate Gaia-ASOI-009. We used the HARPS-N spectrograph at TNG to collect a high-cadence RV time series of the target. We used Markov chain Monte Carlo (MCMC) analyses to refine the Gaia DR3 orbital solution of the companion and, finally, performed a combined model of RV and proper motion anomaly (PMa) to derive the complete 3-D orbit of the companion. We also ran a suite of numerical simulations to confirm our results.

**Results.** We confirm the sub-stellar nature of Gaia-ASOI-009, i.e. Gaia-6 B: from the combined RV+PMa fit, we confirm that it is a high-eccentricity low-mass brown dwarf with  $P_b = 9.37^{+0.06}_{-0.05}$  yr,  $M_b = 19.8 \pm 0.5 M_J$ ,  $e = 0.85$ ,  $i_b = 130^\circ$ . The derived orbital solution differs significantly from the one published in Gaia DR3. Through a series of dedicated simulations, we demonstrate that this discrepancy arises from a degeneracy in the Gaia DR3 astrometric solution. Specifically, the combination of Gaia-6 B long orbital period and high eccentricity, both poorly constrained by the limited timespan of DR3, led to an incorrect solution characterized by a shorter period and lower eccentricity. Finally, we found no evidence of other companions in the system, neither inner nor outer, and thus the origin of the high-eccentricity of Gaia-6 b remains unclear.

**Key words.** planetary systems - techniques: spectroscopic - Astrometry - techniques: radial velocities - stars: individual: HD 128717 – methods: data analysis

### 1. Introduction

In the study of large substellar companions, one of the main questions is whether the object can be classified as an extrasolar planet or as a brown dwarf. In the transition regime, roughly be-

<sup>★</sup> Based on: observations made with the Italian *Telescopio Nazionale Galileo* (TNG), operated on the island of La Palma by the INAF - *Fundación Galileo Galilei* at the *Roque de Los Muchachos* Observatory of the *Instituto de Astrofísica de Canarias* (IAC).

tween 10 and 20  $M_J$ , the answer to this question can be very difficult to find. Traditionally, the threshold between the two types of objects was set at 13  $M_J$ , considered to be the limiting mass for the fusion of deuterium (Boss et al. 2003). However, more recent studies highlighted that the lower-mass limit for deuterium burning might vary between 11 and 16  $M_J$ , depending on the object composition and other factors (e.g. Mollière & Mordasini 2012; Schneider 2018). Other studies suggest using the formation mechanisms to distinguish the two populations of companions (e.g. Chabrier et al. 2014), defining as brown dwarfs the companions formed via gravitational instability (e.g. Boss & Kanodia 2023), and as exoplanets those formed via core-nucleated or pebble-assisted accretion within a disk (e.g. Mordasini et al. 2012b). Unfortunately, these definitions are difficult to apply on observed companions, because the formation history is difficult to infer from observed properties, as different formation models can produce similar outcomes. Moreover, the number of currently known substellar companions on the transition regime between BD and GP with precisely measured orbital parameters is still very limited. Most of the currently known long-period objects come from RV surveys, which means that the true mass is unknown, making it extremely difficult to unveil their true nature.

The advent of ESA’s Gaia mission (Gaia Collaboration et al. 2016) provides a promising new avenue for overcoming these limitations. Gaia’s astrometric capabilities enable precise measurements of stellar positions and motions, making it a powerful tool for detecting the gravitational influence of substellar companions, especially in intermediate to long-period orbits. In particular, astrometric data from Gaia complement RV measurements by offering an independent method for determining the true mass and orbital parameters of companions. The extended Gaia mission now holds the potential to detect GPs and low-mass BDs out to distances of 3-5 AU, for stars of 0.3-1  $M_\odot$ , a critical regime for understanding the transition between these two classes of objects. The first astrometric results from Gaia (Gaia Collaboration et al. 2023b), including detections of substellar companions, are already providing valuable insights into the demographics of these systems, with a few thousand orbits of substellar companion candidates having been published as part of Gaia Data Release (DR) 3 (Gaia Collaboration et al. 2023a). This unprecedented dataset, combined with complementary RV data, sets the stage for a new phase in exoplanet research, offering a more complete view of system formation and evolution.

The first two confirmed Gaia exoplanets were transiting hot-Jupiters detected in the photometry, Gaia-1b and Gaia-2b (Panahi et al. 2022). Then, Sozzetti et al. (2023) announced the confirmation of the first astrometric Gaia candidate, Gaia-3b, a super-Jupiter on a 300 d period orbit. However, later internal investigation of the Gaia pipeline revealed that the time-series for this target suffered from a software bug and that the orbital solution published in Gaia DR3 was a false positive<sup>1</sup>. Since the RV planetary signal is confirmed, Gaia-3b still represents a Gaia-enabled discovery, as the target would likely not have been monitored without its initial identification as an astrometric candidate<sup>2</sup>. Finally, Stefánsson et al. (2025) announced the confirmation of two more astrometric Gaia planet candidates, Gaia-4b and Gaia-5b, identified as a massive planet (11.8  $M_J$ ) at  $P = 571.3$  d and a low-mass brown dwarf (20.9  $M_J$ ) at  $P = 358.58$  d. These com-

panions were confirmed by combining RV measurements from the Habitable-zone Planet Finder (HPF), NEID, and FIES spectrographs.

In this context, we present results from an intensive high-precision RV monitoring campaign of another Gaia astrometric planet candidate, Gaia-ASOI-009 (aka HD 128717). The object is part of the publicly available Gaia candidate exoplanet list<sup>3</sup>. The Gaia DR3 archive reports a value of the RUWE<sup>4</sup> statistic of 1.32, formally below the threshold of 1.4 adopted for systematically attempting to perform orbital fits to Gaia DR3 astrometric time-series. The Gaia DR3 solution type, ‘OrbitalTargetedSearch’, corresponds to one of the orbital solutions obtained as part of an analysis performed on a supplementary external input list, as described in detail in Holl et al. (2023) and Gaia Collaboration et al. (2023a). We observed HD 128717 within the context of the Global Architecture of Planetary Systems collaboration (GAPS, Covino et al. 2013; Desidera et al. 2013) with the HARPS-N spectrograph (Cosentino et al. 2012) at Telescopio Nazionale Galileo (TNG). The target was included in the target list of the original GAPS programme, with a tailored observing strategy designed upon release of the Gaia DR3 orbital solution. HD 128717 was then included in the ongoing large program ‘The Great HARPS-N hunt for super-Earths and Neptunes interior to outer giant planets detected by Gaia’. This program focuses on confirming astrometric long-period exoplanets and brown dwarfs and, through subsequent high-cadence follow-up, on searching for inner low-mass planets in the observed systems. A full description of the program will be provided in an upcoming paper (Barbato et al., in prep.). We present a detailed analysis of the RV dataset collected within the program, as well as combined analysis with the available Gaia DR3 and Hipparcos astrometry, to confirm the orbital solution, along with a set of simulations to confirm the planetary nature of the candidate.

In Sect. 3 and 2, we present the new stellar parameters derived for the target from the HARPS-N spectra and the RV data collected for this study, respectively. In Sect. 4, we present the Keplerian fits of the RV time series and the combined analysis of RVs and astrometric data. In Sect. 5, we present our simulations of Gaia observations, and in Sect. 6 we combine the PMa astrometric information with our RV data to perform a joint modelling of the orbit. In Sect. 7, we discuss our results and the follow-up imaging observations we performed. Finally, in Sect. 8 we summarise our findings.

## 2. Spectroscopic HARPS-N data

As part of the GAPS RV programme, HD 128717 was observed with HARPS-N from BJD = 2459735.6 (5 June 2022) to BJD = 2460686.7 (11 January 2025). 106 spectra were collected in total, over a time span of 951 days. These spectra were reduced with version 3.7.1 of the HARPS-N DRS (data reduction software) pipeline, maintained by the Italian Centre for Astronomical Archive (IA2)<sup>5</sup>. All observations were collected with an integration time of 600 s, to average out potential short-term periodic oscillations of the star (Dumusque et al. 2011) and to obtain a sufficient per-pixel signal-to-noise ratio (average  $S/N = 40$  at 550 nm).

The RV measurements were derived using the Template Enhanced Radial velocity Reanalysis Application (TERRA,

<sup>1</sup> <https://www.cosmos.esa.int/web/gaia/dr3-known-issues#FalsePositive>

<sup>2</sup> This, however, should be regarded as a statistical exception rather than an expected outcome.

<sup>3</sup> <https://www.cosmos.esa.int/web/gaia/exoplanets>

<sup>4</sup> Renormalized Unit Weight Error, a standard diagnostic of the departure from a good single-star fit to Gaia astrometry.

<sup>5</sup> <https://ia2.inaf.it>

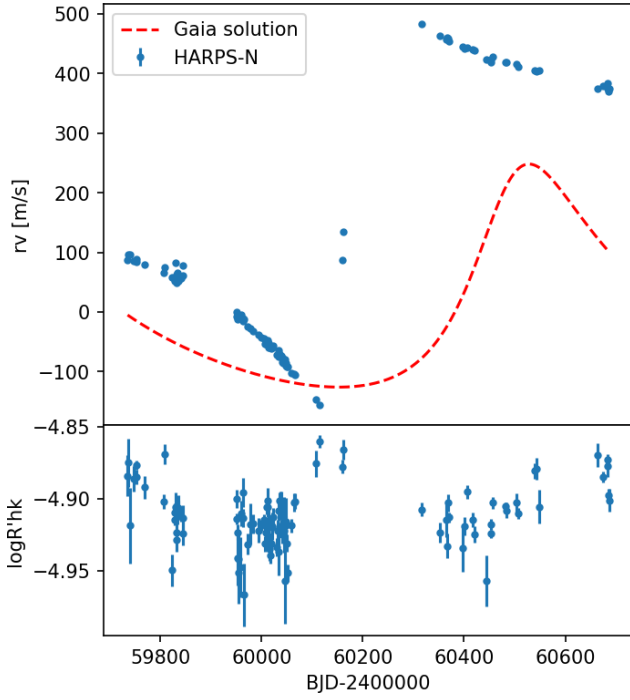


Fig. 1: *Upper panel*: HARPS-N RV time series of HD 128717 (blue points), compared with the predicted RV signals from the Gaia orbital solution (red dashed line). *Lower panel*: HARPS-N  $\log R'_{\text{HK}}$  time series.

Anglada-Escudé & Butler 2012). The resulting RV time series has a median error of  $\sigma_{\text{RV}} = 1.6 \text{ m s}^{-1}$  and a rms of  $196.7 \text{ m s}^{-1}$ . The RV dataset is shown in Fig. 1. The complete time series of all spectroscopic data used in this work will be available at the CDS.

The figure also shows the expected RV signal corresponding to the best-fit orbital solution for HD 128717 b from Gaia DR3 (Gaia Collaboration et al. 2023a). The DR3 orbital parameters are listed in Table 1. The table lists, along with the parameters available in the `gaiadr3.nss_two_body_orbits` and `gaiadr3.binary_masses` tables at the Gaia archive<sup>6</sup>, the derived value of the Campbell elements, as well as the values of the minimum mass  $m_b \sin i$  and RV semi-amplitude  $K_b$ . As can be seen, there is a clear inconsistency between the predicted planetary signal and the HARPS-N observations, both in amplitude and phase. It is worth noticing that the orbital period listed in Table 1 corresponds to the 34 months timespan of Gaia DR3: this might suggest an underestimated period due to insufficient phase coverage. This discrepancy will be discussed in detail in the following Sections.

### 3. Stellar properties

We derived the effective temperature ( $T_{\text{eff}}$ ), the surface gravity ( $\log g$ ), the microturbulence velocity ( $\xi$ ), and the iron abundance ( $[\text{Fe}/\text{H}]$ ) using the equivalent width method to the co-added spectrum of the target (see Biazzo et al. 2022 for details). We considered the MOOG code (Sneden 1973; version 2019), the iron line list by Biazzo et al. (2022), and the ATLAS9+ODFNEW (Castelli & Kurucz 2003) grids of model atmospheres. Briefly,  $T_{\text{eff}}$  was measured by imposing the excitation equilibrium of Fe I lines,  $\log g$  through the ionization equilibrium between Fe I

Table 1: Gaia DR3 orbital solution for ASOI-009 from Gaia Collaboration et al. (2023a):  $M_*$  and  $M_b$  from `gaiadr3.binary_masses`;  $P_b$ ,  $e_b$ ,  $t_p$ , A, B, F, and G from `gaiadr3.nss_two_body_orbits`; Campbell elements and RV parameters derived here.

Parameter	HD 128717
$M_*$ [ $M_{\odot}$ ]	$1.128^{+0.058}_{-0.160}$
$M_b$ [ $M_J$ ]	10.0
$P_b$ [d]	$1090 \pm 310$
$e_b$	$0.39 \pm 0.19$
$t_p - 2016.0$ [d]	$-180 \pm 290$
A [mas]	$0.16 \pm 0.13$
B [mas]	$0.25 \pm 0.16$
F [mas]	$-0.25 \pm 0.18$
G [mas]	$0.18 \pm 0.18$
<i>Campbell elements</i>	
$a_0$ [mas]	$0.47 \pm 0.14$
$\omega$ [deg]	$324 \pm 58$
$\Omega$ [deg]	$91 \pm 50$
$i$ [deg]	$67 \pm 19$
<i>RV parameters</i>	
$m_b \sin i$ [ $M_J$ ]	$8.7 \pm 1.6$
$K_b$ [ $\text{m s}^{-1}$ ]	$185 \pm 53$

and Fe II lines, while  $\xi$  was obtained by removing the trend between the Fe I abundances and the reduced equivalent width  $REW = \log(EW/\lambda)$ . From this we found  $T_{\text{eff}} = 6320 \pm 40 \text{ K}$ ,  $\log g = 4.37 \pm 0.13$ , and  $[\text{Fe}/\text{H}] = 0.16 \pm 0.08$ .

Moreover, adopting a macroturbulence velocity of  $4.7 \text{ km s}^{-1}$  by Doyle et al. (2014), we also derived the projected rotational velocity  $v \sin i_* = 6.1 \pm 0.5 \text{ km s}^{-1}$  through the spectral synthesis technique applied to three different wavelength regions of the co-added spectrum (see Biazzo et al. 2022 for the procedure).

We also detected the presence of the lithium line at  $6707.8 \text{ \AA}$ , deriving an equivalent width of  $67.0 \pm 1.0 \text{ m\AA}$ . Adopting our spectroscopic parameters measured above, we obtain a lithium abundance of  $\log(N_{\text{Li}})_{\text{NLTE}} = 2.78 \pm 0.02 \text{ dex}$ , after correcting for non-local thermodynamical equilibrium effects (Lind et al. 2009). This high lithium abundance might suggest a young stellar age, which will be discussed in Sect. C.

We determined the stellar mass, radius, and age by simultaneously modelling the stellar spectral energy distribution (SED) and the MESA Isochrones and Stellar Tracks (Paxton et al. 2015) through the EXOFASTv2 differential evolution Markov chain Monte Carlo tool (see Eastman 2017; Eastman et al. 2019 and Naponiello et al. 2025 for more details). To sample the SED, we used the available Tycho-2  $B_T$  and  $V_T$ , 2MASS  $J$ ,  $H$ , and  $K_s$ , and WISE  $W1$ ,  $W2$ ,  $W3$ , and  $W4$  magnitudes (see Table 2 and Fig. 2). We imposed Gaussian priors on the  $T_{\text{eff}}$  and  $[\text{Fe}/\text{H}]$  from the spectral analysis above, as well as on the Gaia DR3 parallax. From the medians and 16<sup>th</sup>–84<sup>th</sup> percentiles of the posterior distributions we found  $M_* = 1.212^{+0.058}_{-0.068} M_{\odot}$ ,  $R_* = 1.248 \pm 0.024 R_{\odot}$ , and age  $t = 1.9^{+1.9}_{-1.3} \text{ Gyr}$ ; the corresponding  $\log g$  is fully consistent with the spectroscopic  $\log g$  determined from the spectral analysis. All the parameters of the host star are given in Table 2.

<sup>6</sup> <https://gea.esac.esa.int/archive/>

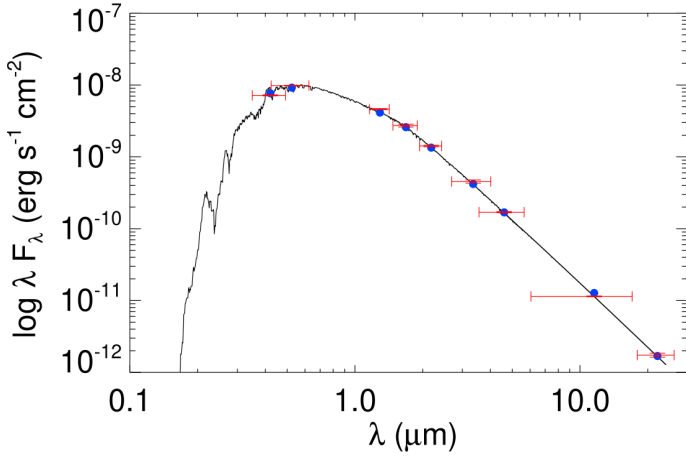


Fig. 2: Stellar spectral energy distribution (SED). The broadband measurements from the Tycho, 2MASS and WISE magnitudes are shown in red and the corresponding theoretical values with blue circles. The unaveraged best-fit model is displayed with a black solid line.

#### 4. Spectroscopic data analyses

In this section, we discuss the Keplerian fits of the RV time series of HD 128717. We also present the ancillary analyses of the spectroscopic activity indices, performed to confirm the Keplerian RV signal. We will first present a blind analysis of the spectroscopic data, as would be performed to discover and characterize the RV signal from an unknown planetary candidate. We will then discuss the combination of the astrometric Gaia DR3 candidate solution and the spectroscopic information, for a complete characterization of the orbital parameters.

The identification of periodic signals in the RV (or activity) time series was performed by means of the generalised Lomb-Scargle periodogram (GLS, Zechmeister & Kürster 2009). The Keplerian signal was then fully characterized using a Markov chain Monte Carlo (MCMC) approach, specifically employing the emcee Affine Invariant MCMC Ensemble sampler developed by Foreman-Mackey et al. (2013). We included offset and jitter terms to take into account instrumental effects, and also tested a multi-Keplerian model and a linear RV trend to evaluate the presence of additional companions in the system. The model comparison was performed via the Bayesian information criterion (BIC, Schwarz 1978). The adopted analysis approach is the same as in Pinamonti et al. (2023).

##### 4.1. Periodogram analyses

Fig. 3 shows the GLS periodograms of the RV and  $\log R'_{\text{HK}}$ . The RV periodogram identified as the strongest periodic signal at  $f = 0.000999 \pm 0.000025 \text{ d}^{-1}$  ( $P = 1001 \pm 25 \text{ d}$ ), with an amplitude  $K = 266.1 \pm 7.0 \text{ m s}^{-1}$ , and a bootstrap false alarm probability,  $\text{FAP} < 10^{-4}$  (Endl et al. 2001). It is worth noticing that, as apparent from Fig. 1, the RV signal present in the time series is highly non-sinusoidal, and thus the sine-wave fitting performed by GLS is a poor match to the data. Nevertheless, the period shows good correspondence with the value from Gaia DR3 (see Tab. 1).

The amplitude of the signal is much larger than the value derived from the astrometric orbital parameters, i.e.  $K \simeq 74 \text{ m s}^{-1}$ , as observed in Fig. 1. The  $\log R'_{\text{HK}}$  periodogram shows a significant periodicity at  $P = 460 \text{ d}$ . This however, does not appear to

Table 2: Stellar parameters of HD 128717, and orbital solution for HD 128717 from Gaia DR3.

Parameter	HD 128717	Reference
<i>Astrometric parameters</i>		
$\alpha$ (J2000)	$14^{\text{h}}:36^{\text{m}}:21.3^{\text{s}}$	(a)
$\delta$ (J2000)	$+57^{\circ}:33':38.4''$	(a)
$\mu_{\alpha}$ [mas yr $^{-1}$ ]	$-82.125 \pm 0.022$	(a)
$\mu_{\delta}$ [mas yr $^{-1}$ ]	$67.259 \pm 0.025$	(a)
$\pi$ [mas]	$13.560 \pm 0.022$	(a)
RUWE	1.32	(a)
d	$73.74 \pm 0.12 \text{ pc}$	This work
<i>Photometric parameters</i>		
$B - V$ [mag]	0.627	(b)
$B_{\text{T}}$ [mag]	$8.981 \pm 0.018$	(b)
$V_{\text{T}}$ [mag]	$8.354 \pm 0.012$	(b)
$G$ [mag]	$8.2003 \pm 0.0028$	(a)
$J$ [mag]	$7.309 \pm 0.021$	(c)
$H$ [mag]	$7.078 \pm 0.049$	(c)
$K$ [mag]	$7.039 \pm 0.029$	(c)
$W1$ [mag]	$6.954 \pm 0.056$	(d)
$W2$ [mag]	$7.041 \pm 0.020$	(d)
$W3$ [mag]	$7.049 \pm 0.016$	(d)
$W4$ [mag]	$7.028 \pm 0.068$	(d)
$A_{\text{V}}$ [mag]	$< 0.038$	This work
<i>Stellar parameters</i>		
$T_{\text{eff}}$ (spec.) [K]	$6210 \pm 40$	This work
$\log g$ (spec.) [cgs]	$4.37 \pm 0.13$	This work
$V_{\text{micro}}$ [km s $^{-1}$ ]	$1.22 \pm 0.05$	This work
[Fe/H] [dex]	$0.16 \pm 0.08$	This work
$v \sin i_{\star}$ [km s $^{-1}$ ]	$6.1 \pm 0.5$	This work
$EW_{\text{Li}}$ [mÅ]	$67.0 \pm 1.0$	This work
$\log(N_{\text{Li}})_{\text{NLTE}}$ [dex]	$2.78 \pm 0.02$	This work
$M_{\star}$ [ $M_{\odot}$ ]	$1.212^{+0.058}_{-0.068}$	This work
$R_{\star}$ [ $R_{\odot}$ ]	$1.248 \pm 0.024$	This work
$\rho_{\star}$ [g cm $^{-3}$ ]	$0.879^{+0.065}_{-0.068}$	This work
$\log g$ (track) [cgs]	$4.329^{+0.025}_{-0.030}$	This work
$\log L_{\star}/L_{\odot}$	$0.322^{+0.014}_{-0.015}$	This work
$\log R'_{\text{HK}}$	$-4.948 \pm 0.020$	This work
Age [Gyr]	$1.4 \pm 0.3$	Sect. C

**Notes.** <sup>(a)</sup> Gaia Collaboration et al. (2023b) ; <sup>(b)</sup> Høg et al. (2000) ; <sup>(c)</sup> Cutri et al. (2003) ; <sup>(d)</sup> Cutri et al. (2021)

be connected with the RV signal, as the two time series show a very low Pearson (Spearman) correlation,  $\rho = 0.21$  ( $r_s = 0.25$ ), as shown in Fig. 4. The only other significant peak in the  $\log R'_{\text{HK}}$  periodogram is at  $P \simeq 230 \text{ d}$ , close to half the first peak period. After removing these two signals, no other significant peak is found.

As an additional test of the influence of stellar activity on the RV time series, we tested the correlation between the  $\log R'_{\text{HK}}$  and the residuals of the 1-Keplerian model (see Sect. 4.2). The correlation appears to be only slightly higher than in the original time series,  $\rho = 0.26$  ( $r_s = 0.29$ ), as shown in Fig. 5. This again

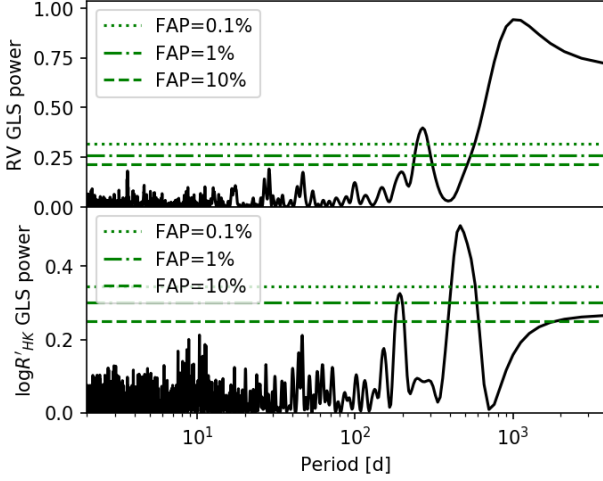


Fig. 3: GLS periodograms of the spectroscopic time series. *Upper panel*: RV; *Lower panel*:  $\log R'_{\text{HK}}$ .

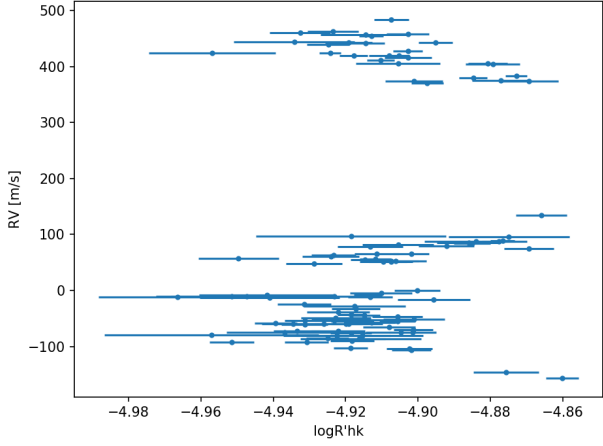


Fig. 4: RV-activity correlation: RV time series as a function of  $\log R'_{\text{HK}}$ .

does present evidence for a strong stellar influence on the RV data.

#### 4.2. MCMC RV Keplerian fit

We then fitted a Keplerian orbit to the HARPS-N RV time series, via the MCMC framework described above. We adopted uninformative uniform priors for the Keplerian parameters, semi-amplitude  $K_b$ , orbital period  $P_b$ , and time of periastron passage  $T_{p,b}$ , as listed in Table 3. For the eccentricity and argument of periastron we followed the  $\sqrt{e} \cos \omega$  and  $\sqrt{e} \sin \omega$  parametrization from Eastman et al. (2013). The RV model and residuals are shown in Fig. 6. From this model, we obtained an amplitude of  $K_b = 321.9^{+3.6}_{-3.4} \text{ m s}^{-1}$ , a period of  $P_b = 2607^{+84}_{-79} \text{ d}$ , and an eccentricity of  $e_b = 0.8061^{+0.0064}_{-0.0065}$ , corresponding to a minimum mass of  $M_b \sin i = 14.67^{+0.50}_{-0.51} M_J$ . The complete posterior distributions of the model are shown in Fig. F.1. These values are significantly different from the Gaia DR3 solution, with the longer period and higher eccentricity resulting in a larger mass, at the threshold between giant planets and brown dwarfs.

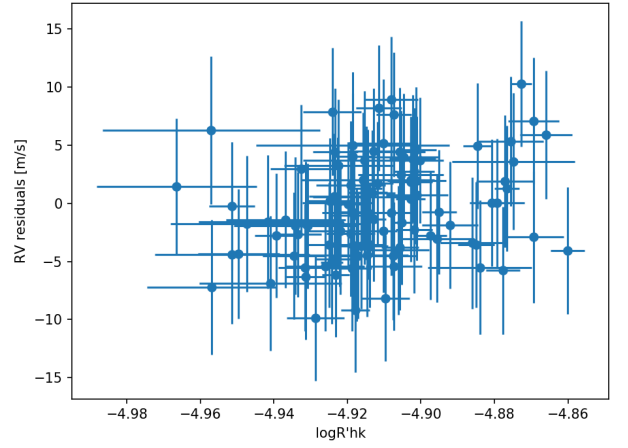


Fig. 5: RV-activity correlation: RV residuals time series as a function of  $\log R'_{\text{HK}}$ .

Two outliers can be identified in the RV residuals in Fig. 6, more than  $3\sigma$  away from the median. These data do not stand out in the  $\log R'_{\text{HK}}$  time series shown in Fig. 1, so we checked additional indicators to identify the source of these outliers. Checking other CCF activity indicators, the second epoch (BJD=2459844.32) stands out as an outlier in the FWHM and BIS time series (see Appendix A), while the first (BJD=2459830.33) was taken during a night of bad weather and very variable seeing. We thus decided to remove both these epochs in all the following analyses to avoid contaminations in the subsequent tests. We then performed a GLS periodogram on the RV residuals to test the presence of additional signal, planetary or stellar, in the time series. As shown in Fig. 7, no significant signal was found.

#### 4.3. Additional RV models

Although no significant peak was found in the GLS periodogram of the residuals, we tested a few additional MCMC models to investigate in depth the presence of potential additional signals in the data. We also tested an additional fit to see if the Gaia DR3 orbital solution could be reconciled with the results of our RV Keplerian model.

##### 4.3.1. Long-term trend model

We also tested the presence of additional long-period signals in the data in the form of a linear acceleration term added to the model,  $d \cdot (t - \bar{t})$ . As listed in Table 3, this model shows a worse BIC than the previous one without the linear trend ( $\Delta\text{BIC} = +5$ ). Moreover, the best-fit value for the acceleration term is not significantly different from zero. For these reasons, we decided to discard this model and adopt as final model the previous one.

##### 4.3.2. Two-Keplerian model

As an additional test on the presence of short-period companions in the system, we run an MCMC 2-Keplerian model, with wide priors for the second Keplerian period,  $P_c \in \mathcal{U}(1.5, 100) \text{ d}$  (model not shown). The MCMC did not converge to any significant periodicity, and the 2-Keplerian model is statistically disfavoured with respect to the 1-Keplerian one ( $\Delta\text{BIC} = +5$ ).



Table 3: Priors and best-fit parameters for the MCMC models tested in Sect. 4.

	RV 1-Keplerian Priors	RV 1-Keplerian Values	RV 1-Keplerian + trend Values
$K_b$ [m s <sup>-1</sup> ]	$\mathcal{U}(0,1000)$	$321.9^{+3.6}_{-3.4}$	$321.2^{+3.8}_{-3.6}$
$P_b$ [d]	$\mathcal{U}(500,3000)$	$2607^{+84}_{-79}$	$2423^{+365}_{-34}$
$T_{p,b}$ [BJD-2450000]	$\mathcal{U}(9700,10500)$	$10158.73^{+0.59}_{-0.60}$	$10158.83^{+0.60}_{-0.61}$
$\sqrt{e_b} \cos \omega_b$	$\mathcal{U}(-1,1)$	$-0.236^{+0.011}_{-0.011}$	$-0.232^{+0.012}_{-0.012}$
$\sqrt{e_b} \sin \omega_b$	$\mathcal{U}(-1,1)$	$-0.8660^{+0.0048}_{-0.0047}$	$-0.861^{+0.011}_{-0.009}$
$M_b \sin i$ [ $M_J$ ]		$14.67^{+0.50}_{-0.51}$	$14.59^{+0.52}_{-0.52}$
$a_b$ [AU]		$3.95^{+0.11}_{-0.10}$	$3.76^{+0.37}_{-0.35}$
$e_b$		$0.8061^{+0.0064}_{-0.0065}$	$0.796^{+0.018}_{-0.020}$
$\omega_{\star,b}$ [rad]		$-1.837^{+0.013}_{-0.013}$	$-1.834^{+0.013}_{-0.013}$
$\gamma_{\text{HARPS-N}}$ [m s <sup>-1</sup> ]	$\mathcal{U}(-50.0,250.0)$	$238.14^{+1.01}_{-0.99}$	$237.2^{+1.9}_{-1.9}$
$\sigma_{\text{jit,HARPS-N}}$ [m s <sup>-1</sup> ]	$\mathcal{U}(0,100)$	$5.22^{+0.44}_{-0.39}$	$5.22^{+0.44}_{-0.38}$
$d$ [m s <sup>-1</sup> d <sup>-1</sup> ]	$\mathcal{U}(-0.05,0.05)$	-	$0.010^{+0.024}_{-0.019}$
BIC		688	693

**Notes.** The best RV model is highlighted in bold.

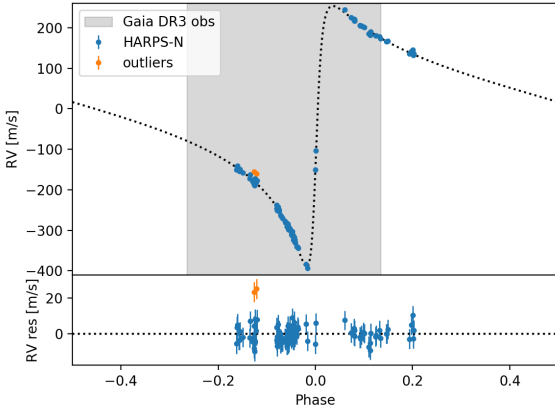


Fig. 6: Phase-folded best-fit RV one-Keplerian model, corrected for the instrumental offset (top panel) and the RV residuals (bottom panel). The orange dots represents the outliers discussed in Sect. 4.2, while the gray-shaded area represent the phase coverage of Gaia DR3 observations.

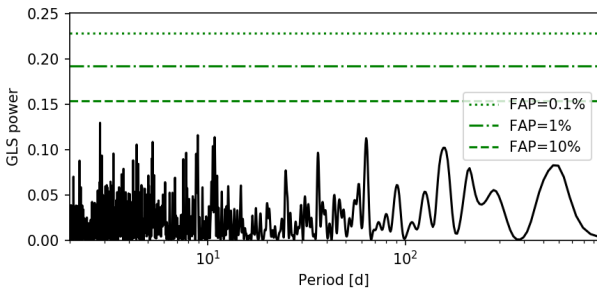


Fig. 7: GLS periodogram of the RV residuals of the Keplerian model.

## 5. Gaia simulations

To further study the discrepancy between the RV and astrometric solutions, we performed a suite of numerical simulations: we produced a set of realistic Gaia astrometric time series, injecting possible realizations of a Keplerian signal corresponding to the RV orbital fit, and studied the orbital solutions recovered by fitting these synthetic astrometric data. This could help us explain why the Gaia DR3 solution was so different from our findings, and furthermore study whether Gaia DR4 could help us confirm our results or not.

The setup of this simulation is the same as in Sozzetti et al. (2023) and Ruggieri et al. (2024): we use GOST<sup>7</sup> to obtain the Gaia observation information (observation time, scan angle, and parallax factor) and take the 5-parameter stellar motion solution from Gaia DR3. We take the RV orbital parameters from our HARPS-N solution, drawing them from a Gaussian distribution, and we generate the longitude of the ascending node,  $\Omega$ , drawn from a uniform distribution  $[0, \pi]$ , and the inclination,  $i$ , drawn from a uniform distribution of  $\cos i \in [-1, 1]$ .

### 5.1. DR3 simulations

We simulated the Gaia DR3 time series obtaining from GOST all the Gaia observations of HD 128717 from July 2014 to May 2017 (Gaia Collaboration et al. 2021). As measurement error, we adopted  $\sigma = 150 \mu\text{as}$ , which is representative of the DR3 astrometric uncertainties for a star of magnitude  $G = 8.2$  (Holl et al. 2023).

We produced 100 realizations of the astrometric time series, and fitted each with a partly linearised model (Holl et al. 2023) implemented with emcee. The best-fit values of the inclination,  $i$ , and astrometric semi-major axis,  $a_0$ , compared with the injected values, are shown in Fig. 8. We can see that, although there is a partial correspondence between the injected and re-

<sup>7</sup> Gaia Observation Forecast Tool - <https://gaia.esac.esa.int/gost/index.jsp>

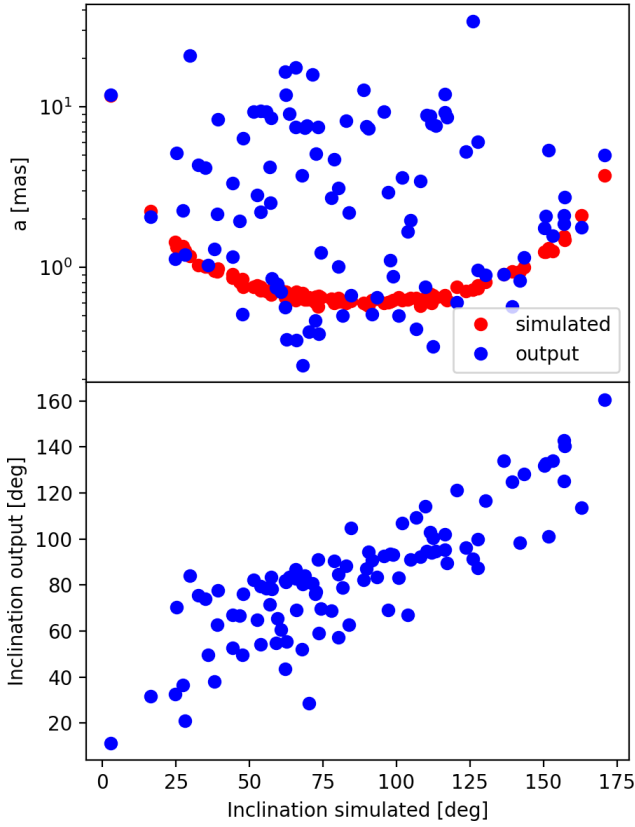


Fig. 8: Astrometric simulation results for DR3. *Upper panel*: simulated (red) and derived (blue) astrometric semimajor axis vs injected orbital inclination; *Lower panel*: derived inclination vs. simulated value.

covered values of  $i$  (lower panel Fig. 8), the semi-major axis  $a_0$  is almost never recovered correctly (upper panel Fig. 8), which implies also that the orbital period is very hard to constrain from the DR3 astrometric data. This is highlighted in Fig. 9, where the distributions of period and eccentricity are compared with the values from the RV and Gaia DR3 orbital solutions. We can see that the distributions do not resemble the RV values, although they were used to generate the synthetic time series, and are very wide. In particular, the eccentricity peaks at lower values, close to the value of  $e = 0.39$  obtained by Gaia DR3. If we compute how many times the fitted value is within  $1\sigma$  from the RV value of  $P$  and  $e$ , we get 6 and 3 times out of a total of 100 simulations, respectively. For the Gaia DR3 solution, we fall within  $1\sigma$  10 and 42 times, respectively. So we can see that, even if there is no clear bias towards the Gaia DR3 orbital solution, it can be easily recovered from the astrometric time series, due to the very wide distribution of the possible solutions. This is not unexpected, since the RV data clearly indicate an orbital period much longer than the duration of DR3 observations and, thus, the signal is very difficult to constrain due to the poor orbital coverage.

## 5.2. DR4 simulations

We then produced a set of 100 Gaia DR4 time series with the GOST observations from July 2014 to December 2019. We adopted as internal uncertainties  $80 \mu\text{as}$ , which is expected to be a representative value for similar stars in DR4 (Brown 2024). We can see in Fig. 10 that the correspondence between the injected

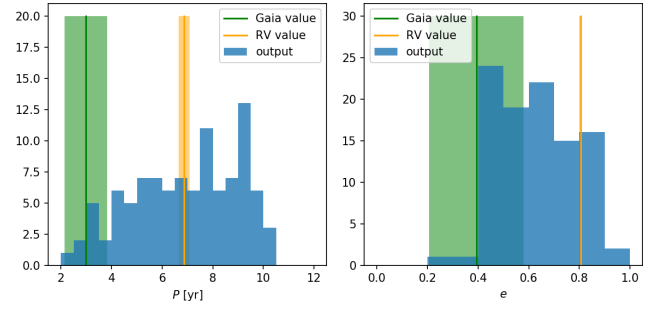


Fig. 9: Distribution of the recovered values of period  $P$ , on the left, and eccentricity  $e$ , on the right, in the DR3 astrometric simulations. The green lines and shaded regions mark the best-fit values and uncertainties from the Gaia DR3 orbital solution, while the orange lines and regions represent our RV solution.

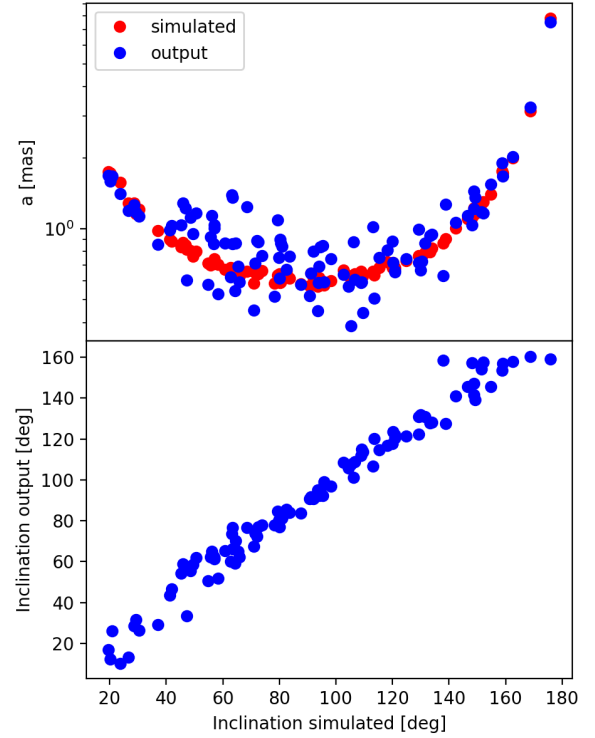


Fig. 10: Astrometric simulation results for DR4. *Upper panel*: simulated (red) and derived (blue) astrometric semimajor axis vs injected orbital inclination; *Lower panel*: derived inclination vs. simulated value.

and recovered values is much better with the DR4 time series, with respect to the previous Section. Although some uncertainty on the semi-major axis remains, the orbital inclination is recovered with great accuracy. In Fig. 11, we can see how the distribution of the output values of  $P$  and  $e$  closely peaks to the RV orbital solution used to produce the datasets. These results show how the current DR3 timespan is insufficient to correctly recover the Keplerian orbit, while the next Data release should have sufficient coverage to accurately recover the companion signal.

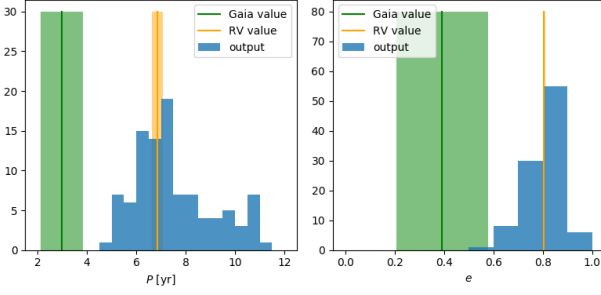


Fig. 11: Distribution of the recovered values of period,  $P$ , and eccentricity,  $e$ , in the DR4 astrometric simulations. The green lines and shaded regions mark the best-fit values and uncertainties from the Gaia DR3 orbital solution, while the orange lines and regions represent our RV solution.

## 6. Combined fit of RVs and absolute astrometry

Table 4: Orbital parameters and true mass for HD 128717 B from the combined RV+absolute astrometry analysis.

Parameter	Prior	Value
$P_b$ [yr]	$\mathcal{U}(5.0, 25.0)$	$9.37^{+0.06}_{-0.05}$
$T_{p,b}$ [yr]	$\mathcal{U}(0.0, 3000.0)$	$2023.6716^{+0.0009}_{-0.0009}$
$a_b$ [au]	$\mathcal{U}(1.0, 10.0)$	$4.85^{+0.02}_{-0.01}$
$e_b$	$\mathcal{U}(0.0, 1.0)$	$0.850^{+0.002}_{-0.002}$
$\omega_b$ [deg]	$\mathcal{U}(0.0, 360.0)$	$-105.7^{+0.4}_{-0.3}$
$i_b$ [deg]	$\cos(i) : \mathcal{U}(-1.0, 1.0)$	$130.3^{+1.6}_{-1.9}$
$\Omega_b$ [deg]	$\mathcal{U}(-180.0, 180.0)$	$131.7^{+3.3}_{-3.4}$
$q_b$	$\mathcal{U}(0.0, 0.1)$	$0.0148^{+0.0004}_{-0.0004}$
$M_b$ [ $M_J$ ]	(derived)	$19.8^{+0.5}_{-0.5}$

As reported in cross-calibrated *Hipparcos-Gaia* catalogues of astrometric accelerations (Brandt 2021; Kervella et al. 2022), HD 128717 is clearly identified as an accelerating star, with a signal-to-noise ratio of the proper motion anomaly (PMA)  $S/N \sim 9$  at the mean epoch of Gaia DR3.

We performed a combined PMA+RV model to the *Hipparcos-Gaia* absolute astrometry of HD 128717 from Brandt (2021) and to the offset-corrected RV dataset in order to determine the possible values of orbital inclination  $i$ , longitude of the ascending node,  $\Omega$ , and mass ratio,  $q$ , which can be directly constrained by the PMA astrometric data. We adopted uninformative priors for the model parameters derived by the RV-only analysis and uniform priors on  $\cos(i)$ ,  $\Omega$ , and  $q$ .

The combined analysis utilizes a differential evolution Markov chain Monte Carlo (DE-MCMC) algorithm (Ter Braak 2006; Eastman et al. 2013), with the PMA model constructed by averaging over the actual observing windows of *Hipparcos* (utilizing the exact time of observation of the target, see van Leeuwen 2007) and *Gaia* DR3 (based on the accurate representation of the actual *Gaia* transit times from GOST. The DE-MCMC analysis was run with standard prescriptions on the burn-in phase and convergence conditions based on the Gelman-Rubin statistics (e.g., Eastman et al. 2013). The medians of the posterior distributions of the model parameters constituted the nominal best-fit values, with  $1\sigma$  uncertainties determined eval-

uating the  $\pm 34$ th percentile intervals of the posteriors (for additional details, see Sozzetti 2023).

Table 4 reports the best-fit orbital solution for HD 128717 B. Usually, applications of the PMA technique (e.g., Li et al. 2021; Sozzetti 2023) return bimodal distributions of the inclination angle, due to the difficulty in separating prograde from retrograde orbits. In this case, instead of being bimodal, the inclination distribution has a single value of  $i_b = 130.3^{+1.6}_{-1.9}$  deg (with a corresponding  $\Omega_b = 131.7^{+3.3}_{-3.4}$  deg), possibly because the time interval encompassed by the Gaia DR3 observations critically samples the high-velocity phase of the very eccentric orbit of HD 128717 B just after periastron passage (see Fig. 6). We obtain a mass ratio  $q_b = 0.0148 \pm 0.0004$  and derive a true mass of  $M_b = 19.8 \pm 0.5 M_J$ . The combined solution indicates that HD 128717 B's orbit has a period about 30% longer and a slightly higher eccentricity than that inferred by the RV-only fit. In Fig. 12 and Fig. 13, we show the joint posteriors of these parameters and the best-fit orbital solution superposed to the observational data, respectively.

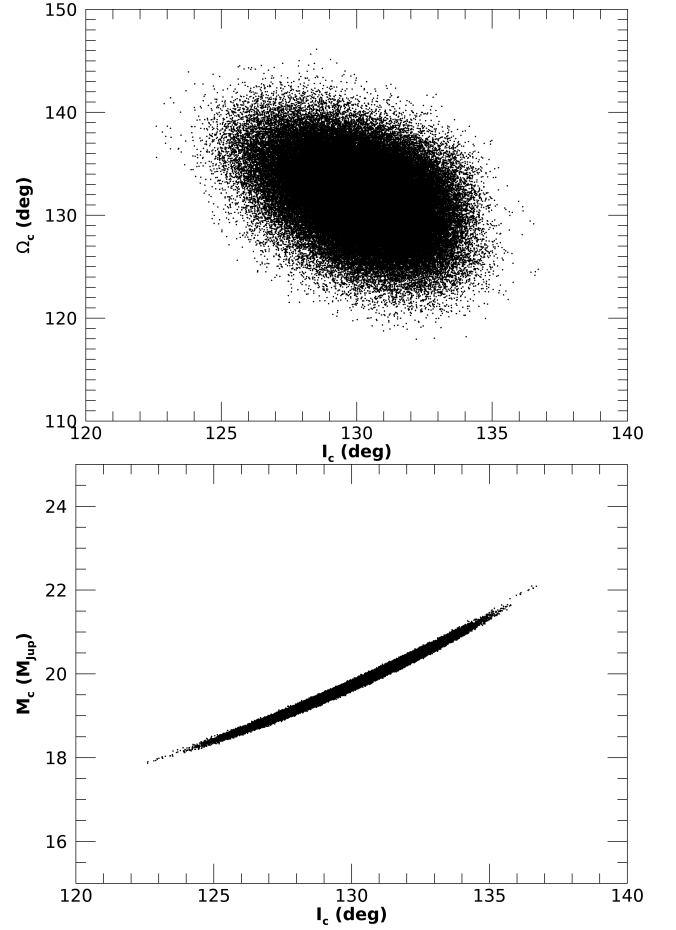


Fig. 12: Joint posterior distributions for inclination, longitude of the ascending node and true mass for HD 128717 B.

## 7. Discussion

In light of the aforementioned analyses, we confirmed the Keplerian nature of Gaia-ASOI-009 b, which is a sub-stellar companion of mass  $M_b = 19.8 \pm 0.5 M_J$ , hereafter Gaia-6 B.



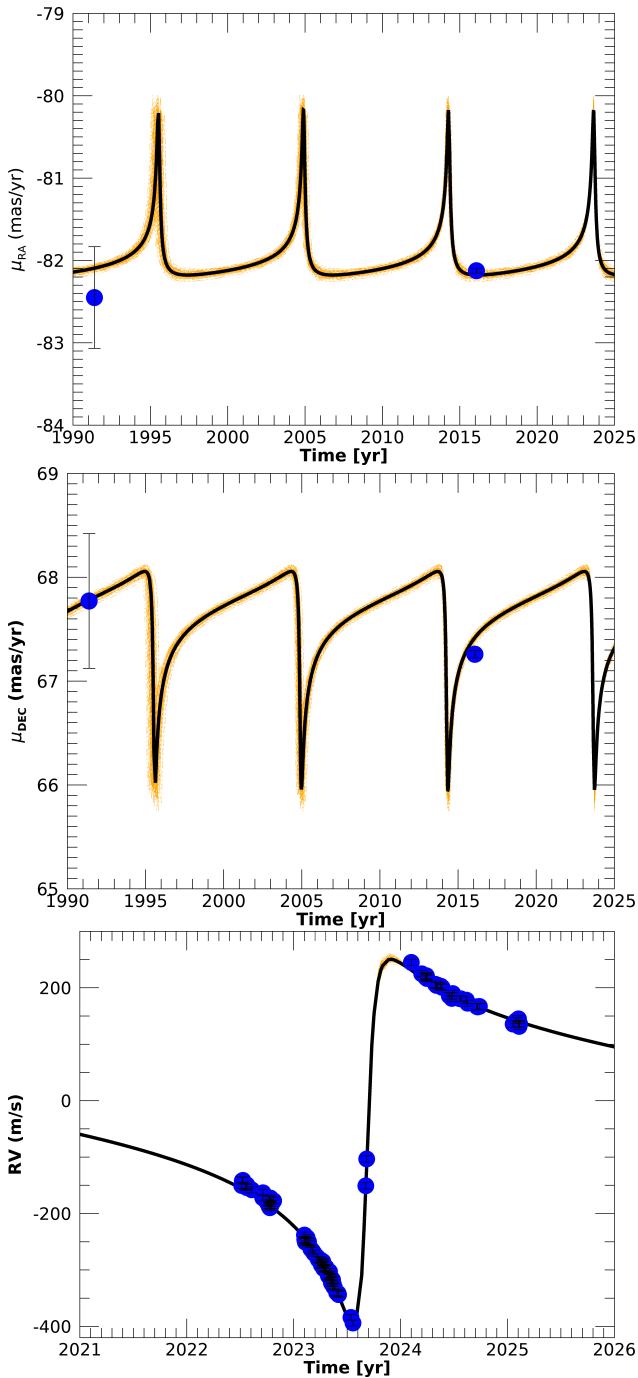


Fig. 13: Best-fit orbital solution (solid black line) for HD 128717 B, superposed to the calibrated proper motions from Hipparcos and *Gaia* (top and middle panels) and to the RV time series (bottom panel). The dashed orange lines represent random selections of orbital solutions drawn from the posterior distributions.

### 7.1. Comparison with Gaia DR3 solution

Thanks to high-precision RV follow-up with the HARPS-N spectrograph of HD 128717, we were able to confirm the presence and substellar nature of the candidate Gaia-ASOI-009 b. Nonetheless, our final Keplerian solution for Gaia-6 B (see Table 4) is significantly different from the one from Gaia DR3 (Table 1). An additional test to see whether the two solutions could be reconciled can be found in Appendix B but, as expected, the ev-

idence from the RV time series is strongly pointing away from the Gaia DR3 solution.

This discrepancy can be explained, as shown by the simulations we carried out and discussed in Sect. 5. As an additional test, we produced 100 Gaia DR3 time series using the orbital parameters from the final PMA+RV solution (Table 4) and compared the likelihood of the simulated data given two different set of parameters from the Keplerian model: those from our PMA+RV fit and those from the Gaia DR3 solution. We find that the two distributions of likelihood are indistinguishable: a Kolmogorov-Smirnov (K-S) test on the likelihood distributions returned a p-value  $p = 96\%$ . Moreover, we see that in 42/100 cases the likelihood of the DR3 solution is higher than that of our final solution. This proves that the Gaia DR3 time series is not able to constrain the orbit of Gaia-6 B. The reason for this is most probably the orbital period of the substellar companion: the timespan of Gaia DR3 observations, i.e. 34 months, is much shorter than the orbital period,  $P_b = 9.37$  yr. This, combined with the high eccentricity of the orbit, results in a strong degeneracy between eccentricity and orbital period, which most likely produced the Gaia DR3 solution.

### 7.2. Giant planet or brown dwarf?

Given its large mass,  $M_b = 19.8 \pm 0.5 M_J$ , the substellar companion identified in the astrometric and RV data lies above the commonly adopted  $13 M_J$  threshold dividing “planets” and “brown dwarfs”, although the exact threshold is somewhat arbitrary (e.g. Stefánsson et al. 2025, and references therein).

We show in Fig. 14 Gaia-6 B compared to the known population of giant planets (GP) and brown dwarfs (BD), as defined in Appendix E. We can see that the mass of the host star is very close to the peak of both the BD and GP distributions. On the other hand, it has a higher-than-average metallicity, close to the peak of the GP distributions. This can open some uncertainty on the nature of the substellar companions, depending on the definition adopted to divide planets from brown dwarfs. Metallicity is commonly seen as a statistical indicator to distinguish between GPs and BDs (e.g. Ma & Ge 2014; Mata Sánchez et al. 2014; Maldonado & Villaver 2017), as it can be correlated with the formation mechanisms: GPs formed via core accretion are more common around metal rich stars (e.g. Osborn & Bayliss 2020), while BDs formed via gravitational instability are independent of metallicity (e.g. Maldonado et al. 2019). From this point of view Gaia-6 B might belong to both populations, being located at the joint between the two populations, but its high metallicity could suggest formation through core accretion. However, its mass is significantly higher than the expected lower-mass limit for deuterium burning ( $11 - 16 M_J$ , Mordasini et al. 2012a), which strongly points towards it being a deuterium-burning brown dwarf.

### 7.3. Search for short-period companions

In Sect. 4.3, we tried to fit additional signals in the RV time series, to test the presence of additional objects in the system. We found no significant signal in the periodogram of the RV residuals, and all other models showed a higher BIC than the single-Keplerian one, i.e. no statistical evidence of a more complex model was found. Nonetheless, small planetary companions could still be undetected in the HARPS-N data. To quantify this, we computed the detection function of the RV data, following the same formalism adopted in Ruggieri et al. (2024) and Sozzetti

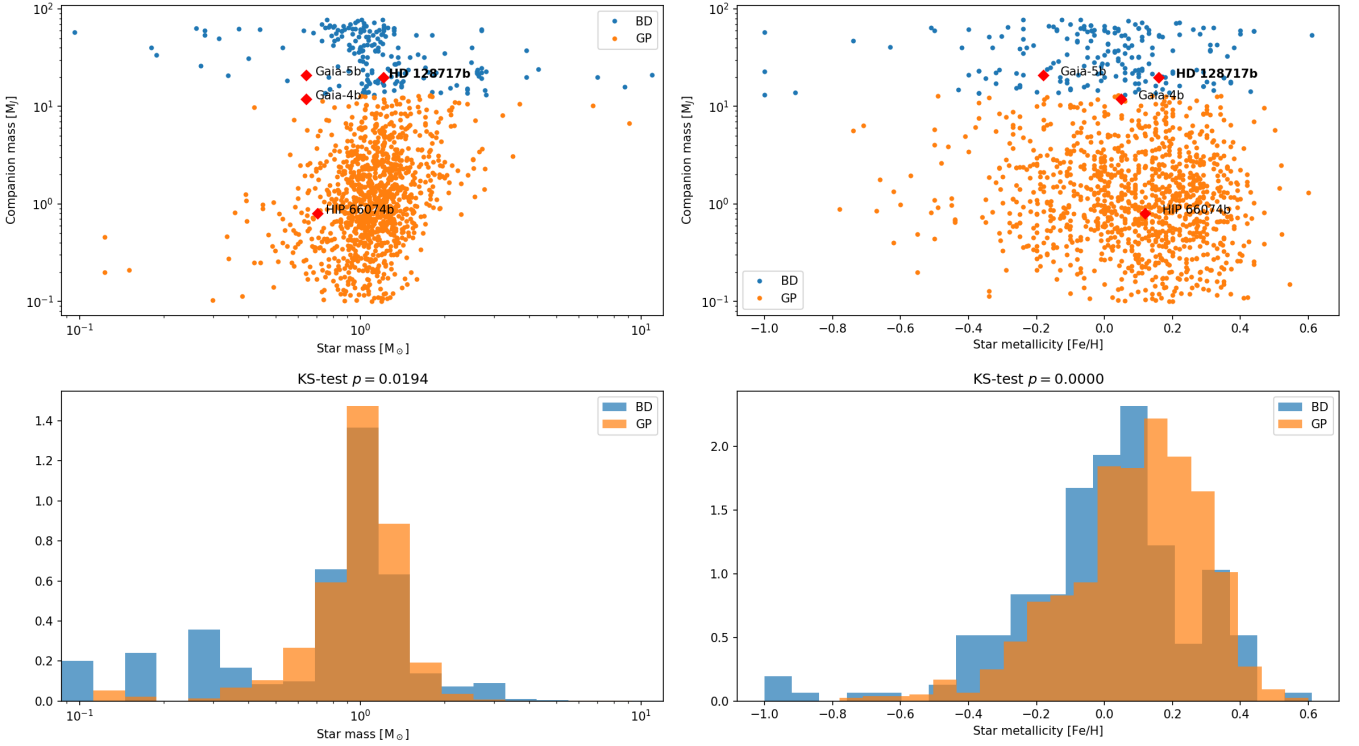


Fig. 14: Masses of giant planets and brown dwarfs as a function of stellar host mass and metallicity, for substellar companions with period  $< 10^4$  d. Brown dwarfs ( $M > 13 M_J$ ) are shown as blue points, while giant planets ( $0.1 < M < 13 M_J$ ) are shown as orange points. The red diamonds highlight the position of confirmed Gaia-ASOI sub-stellar companions (and HIP 66074 B Sozzetti et al. 2023). The lower plots show the stellar mass and metallicity distributions of BD and GP.

et al. (2024). The resulting detection map is shown in Fig. 15. It is worth noticing that low-mass super Earths ( $M_p \sin i \lesssim 10 M_\oplus$ ) would not be detected in our time series, except at the shortest periods. This is in spite of the high-precision, high cadence HARPS-N RV time-series, because of the significant levels of RV jitter.

However, due to the high mass and large eccentricity of Gaia-6 B, many orbital configurations would be unstable. This means that we can rule out the presence of planetary companions even below the detectability threshold. We can compute the orbital stability region using Hill's Criterion (Hamilton & Burns 1992). The region of the period-mass parameter space<sup>8</sup> in which a planet on a circular orbit would be unstable under Hill's Criterion is highlighted in orange in Fig. 15. We can conclude that the only possible undetected planetary companions in the inner regions have  $M_p \sin i \lesssim 10 M_\oplus$  and  $P \lesssim 50$  d.

#### 7.4. Imaging follow-up observations

The high eccentricity of HD 128717 B can be interpreted as the result of orbital excitation caused by a massive companion at large separation. As the orbital coverage provided by our HARPS-N RV data is too low to robustly detect any long-term trend caused by such a distant companion, we searched for any outer companion to HD 128717 with imaging, a detection technique uniquely suited to discover massive companions on large orbits beyond the reach of RV observations.

We observed HD 128717 with SHARK-NIR (Farinato et al. 2022; Marafatto et al. 2022) and LBTI/LMIRCam (Skrutskie

<sup>8</sup> Assuming edge-on orbit,  $\sin i = 1$ .

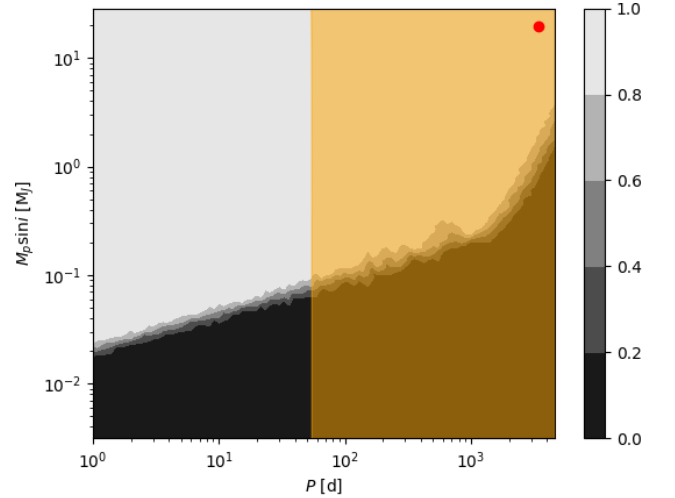


Fig. 15: Detection map for the HARPS-N RV data of HD 128717. The colour scale represents the detection function. The red point shows the position of HD 128717 B in the parameter space. The orange shaded area is the forbidden region due to the Hill stability criterion.

et al. 2010; Leisenring et al. 2012), two infrared imagers mounted on the Large Binocular Telescope (LBT) in Arizona for multi-band simultaneous observations, on April 15 and May 16, 2025. Details of these observations are discussed in Appendix D. In light of the longer duration and better seeing, in the following we will focus on the May 16 observation alone.

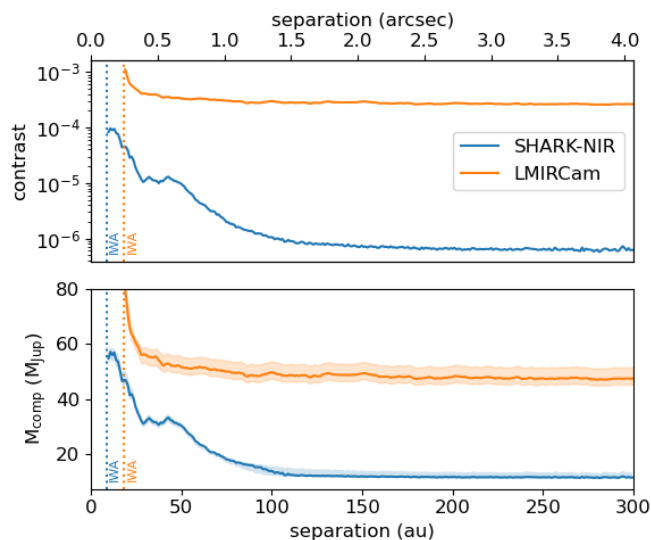


Fig. 16: Contrast curve and mass limits for the SHARK-NIR (blue) and LMIR-Cam (orange) observations of HD 128717 conducted on the night of May 16, 2025 UT. *Top panel*: contrast curve. *Bottom panel*: mass limits, the thick curve corresponding to the nominal 1.40 Gyr stellar age, and the shaded region to the age uncertainty.

No source with a signal-to-noise ratio higher than 4 is present on either of the post-processed images, allowing us to conclude that no companions were successfully detected around HD 128717 during our observations. This non-detection can be used to provide robust limits on the mass of any yet-undetected outer companion in the system. Using the AMES-COND models Allard et al. (2003) and the star host age of  $1.4 \pm 0.3$  Gyr (computed as discussed in Appendix C), we derive mass detection limits for the imaging observations, shown in the bottom panel of Fig. 16. While no low-mass giant planetary companion would have been detectable in our data, our observations would have instead been able to robustly detect any large-separation stellar or brown dwarf companion in the system. Specifically, focusing on the mass limit computed for the nominal age of 1.4 Gyr and orbital separations beyond 60 au, LMIRCam observations in the  $L'$  band are able to exclude the presence of any outer companion more massive than  $\sim 47 M_{\text{Jup}}$ , while SHARK-NIR data in the H band allow for the robust exclusion of any distant companion above  $\sim 11 M_{\text{Jup}}$ .

## 8. Conclusion

We confirmed the substellar nature of the astrometric candidate Gaia-ASOI-009, thanks to high-cadence high-precision RV follow-up with the HARPS-N spectrograph. Gaia-6 B is a high-eccentricity brown dwarf,  $M_b = 19.8 M_J$ ,  $e = 0.85$ , and it is one of the most eccentric brown dwarfs with precisely measured mass known so far (see Fig. E.1). Moreover, we solved the apparent discrepancy between the orbital measurement from Gaia DR3 and the high-precision HARPS-N RV follow-up. This proves the importance of RV follow-up of astrometric candidates to confirm and improve the precision on the orbital parameters.

The origin of the high eccentricity of Gaia-6 B remains an unsolved puzzle, since we did not identify any hint of the presence of other companions in the RV, astrometric, and direct imaging data analysed in this study. This is unexpected, since

all known high-eccentricity ( $> 0.9$ ) planetary companions have identified additional companions on wide orbits (Sozzetti et al. 2023, and references therein) and there is a known link between eccentricity and stellar multiplicity (e.g. Moutou et al. 2017). However, the current data cannot conclusively exclude the presence of small brown-dwarf companions at around a few tens of au, which might still be sufficient to excite Gaia-6 B eccentricity to the observed level. In the future, additional observations, both additional RVs data to expand the temporal baseline and deeper imaging observations to search for smaller companions, will help tighten the constraints on the presence of undetected companions, while in-depth dynamical simulations might help shed light on the possible mechanisms producing such high eccentricity, which might be more common than expected among long-period giant planets and brown dwarfs.

**Acknowledgements.** We acknowledge support from the European Union – NextGenerationEU (PRIN MUR 2022 20229R43BH) and the “Programma di Ricerca Fondamentale INAF 2023”. We acknowledge financial contribution from the INAF Large Grant 2023 “EXO DEMO”. MPi acknowledges support from ASI-INAF agreement no. 2025-10-HH.0 “Partecipazione Italiana al Gaia DPAC - Supporto alle attività di responsabilità del team scientifico”. Tzi acknowledges support from CHEOPS ASI-INAF agreement n. 2019-29-HH.0, NVIDIA Academic Hardware Grant Program for the use of the Titan V GPU card and the Italian MUR Departments of Excellence grant 2023-2027 “Quantum Frontiers”. L.M. acknowledges financial contribution from PRIN MUR 2022 project 2022J4H55R. We acknowledge the Italian center for Astronomical Archives (IA2, <https://www.ia2.inaf.it>), part of the Italian National Institute for Astrophysics (INAF), for providing technical assistance, services and supporting activities of the GAPS collaboration. We thank Tom Herbst of MPIA-Heidelberg (D) and the NIRVANA team for sharing with us part of the NIRVANA instrument control SW to control the motorized axis of SHARK-NIR, and NASA and the PI of JWST/NIRCam [26] Marcia Rieke for allowing us to use one of the NIRCam spare detectors as scientific detector for the SHARK-NIR scientific camera. Eventually, we emphasize that observations have benefited from the use of ALTA Center ([alta.arcetri.inaf.it](https://alta.arcetri.inaf.it)) forecasts performed with the Astro-Meso-Nh model. Initialization data of the ALTA automatic forecast system come from the General Circulation Model (HRES) of the European Centre for Medium Range Weather Forecasts. This research has made use of the NASA Exoplanet Archive, which is operated by the California Institute of Technology, under contract with the National Aeronautics and Space Administration under the Exoplanet Exploration Program, and of data obtained from or tools provided by the portal [exoplanet.eu](https://exoplanet.eu) of The Extrasolar Planets Encyclopaedia. This work has made use of data from the European Space Agency (ESA) mission *Gaia* (<https://www.cosmos.esa.int/gaia>), processed by the *Gaia* Data Processing and Analysis Consortium (DPAC, <https://www.cosmos.esa.int/web/gaia/dpac/consortium>). Funding for the DPAC has been provided by national institutions, in particular the institutions participating in the *Gaia* Multilateral Agreement.

## References

- Agüeros, M. A., Bowsher, E. C., Bochanski, J. J., et al. 2018, *ApJ*, 862, 33
- Allard, F., Guillot, T., Ludwig, H.-G., et al. 2003, in *IAU Symposium*, Vol. 211, Brown Dwarfs, ed. E. Martín, 325
- Almeida-Fernandes, F. & Rocha-Pinto, H. J. 2018, *MNRAS*, 476, 184
- Anglada-Escudé, G. & Butler, R. P. 2012, *ApJS*, 200, 15
- Biazzo, K., D’Orazi, V., Desidera, S., et al. 2022, *A&A*, 664, A161
- Boss, A. P., Basri, G., Kumar, S. S., et al. 2003, in *IAU Symposium*, Vol. 211, Brown Dwarfs, ed. E. Martín, 529
- Boss, A. P. & Kanodia, S. 2023, *ApJ*, 956, 4
- Brandt, T. D. 2021, *ApJS*, 254, 42
- Brown, A. 2024, in *EAS2024*, European Astronomical Society Annual Meeting, 208
- Castelli, F. & Kurucz, R. L. 2003, in *Modelling of Stellar Atmospheres*, ed. N. Piskunov, W. W. Weiss, & D. F. Gray, Vol. 210, A20
- Chabrier, G., Johansen, A., Janson, M., & Rafikov, R. 2014, in *Protostars and Planets VI*, ed. H. Beuther, R. S. Klessen, C. P. Dullemond, & T. Henning, 619–642
- Cosentino, R., Lovis, C., Pepe, F., et al. 2012, in *Proc. SPIE*, Vol. 8446, Ground-based and Airborne Instrumentation for Astronomy IV, 84461V
- Covino, E., Esposito, M., Barbieri, M., et al. 2013, *A&A*, 554, A28
- Cutri, R. M., Skrutskie, M. F., van Dyk, S., et al. 2003, *VizieR Online Data Catalog*, 2246

- Cutri, R. M., Wright, E. L., Conrow, T., et al. 2021, *VizieR Online Data Catalog*, II/328
- Desidera, S., Sozzetti, A., Bonomo, A. S., et al. 2013, *A&A*, 554, A29
- Doelman, D. S., Snik, F., Por, E. H., et al. 2021, *Appl. Opt.*, 60, D52
- Doyle, A. P., Davies, G. R., Smalley, B., Chaplin, W. J., & Elsworth, Y. 2014, *Monthly Notices of the Royal Astronomical Society*, 444, 3592
- Dumusque, X., Cretignier, M., Sosnowska, D., et al. 2021, *A&A*, 648, A103
- Dumusque, X., Lovis, C., Udry, S., & Santos, N. C. 2011, in *IAU Symposium*, Vol. 276, *The Astrophysics of Planetary Systems: Formation, Structure, and Dynamical Evolution*, ed. A. Sozzetti, M. G. Lattanzi, & A. P. Boss, 530–532
- Eastman, J. 2017, EXOFASTv2: Generalized publication-quality exoplanet modeling code, *Astrophysics Source Code Library*, record ascl:1710.003
- Eastman, J., Gaudi, B. S., & Agol, E. 2013, *PASP*, 125, 83
- Eastman, J. D., Rodriguez, J. E., Agol, E., et al. 2019, *arXiv e-prints*, arXiv:1907.09480
- Endl, M., Kürster, M., Els, S., Hatzes, A. P., & Cochran, W. D. 2001, *A&A*, 374, 675
- Espinoza, N., Kossakowski, D., & Brahm, R. 2019, *MNRAS*, 490, 2262
- Farinato, J., Baruffolo, A., Bergomi, M., et al. 2022, in *Society of Photo-Optical Instrumentation Engineers (SPIE) Conference Series*, Vol. 12185, *Adaptive Optics Systems VIII*, ed. L. Schreiber, D. Schmidt, & E. Vernet, 1218522
- Foreman-Mackey, D., Agol, E., Ambikasaran, S., & Angus, R. 2017, *AJ*, 154, 220
- Foreman-Mackey, D., Hogg, D. W., Lang, D., & Goodman, J. 2013, *PASP*, 125, 306
- Gaia Collaboration, Arenou, F., Babusiaux, C., et al. 2023a, *A&A*, 674, A34
- Gaia Collaboration, Brown, A. G. A., Vallenari, A., et al. 2021, *A&A*, 649, A1
- Gaia Collaboration, Prusti, T., de Bruijne, J. H. J., et al. 2016, *A&A*, 595, A1
- Gaia Collaboration, Vallenari, A., Brown, A. G. A., et al. 2023b, *A&A*, 674, A1
- Hamilton, D. P. & Burns, J. A. 1992, *Icarus*, 96, 43
- Høg, E., Fabricius, C., Makarov, V. V., et al. 2000, *A&A*, 355, L27
- Holl, B., Sozzetti, A., Sahlmann, J., et al. 2023, *A&A*, 674, A10
- Johnson, D. R. H. & Soderblom, D. R. 1987, *AJ*, 93, 864
- Kervella, P., Arenou, F., & Thévenin, F. 2022, *A&A*, 657, A7
- Leisenring, J. M., Skrutskie, M. F., Hinz, P. M., et al. 2012, in *Ground-based and Airborne Instrumentation for Astronomy IV*, ed. I. S. McLean, S. K. Ramsay, & H. Takami, Vol. 8446, *International Society for Optics and Photonics (SPIE)*, 84464F
- Li, Y., Brandt, T. D., Brandt, G. M., et al. 2021, *AJ*, 162, 266
- Lind, K., Asplund, M., & Barklem, P. S. 2009, *A&A*, 503, 541
- Ma, B. & Ge, J. 2014, *MNRAS*, 439, 2781
- Maldonado, J. & Villaver, E. 2017, *A&A*, 602, A38
- Maldonado, J., Villaver, E., Eiroa, C., & Micela, G. 2019, *A&A*, 624, A94
- Mamajek, E. E. & Hillenbrand, L. A. 2008, *ApJ*, 687, 1264
- Marafatto, L., Carolo, E., Umbriaco, G., et al. 2022, in *Society of Photo-Optical Instrumentation Engineers (SPIE) Conference Series*, Vol. 12184, *Ground-based and Airborne Instrumentation for Astronomy IX*, ed. C. J. Evans, J. J. Bryant, & K. Motohara, 121843V
- Marois, C., Lafrenière, D., Doyon, R., Macintosh, B., & Nadeau, D. 2006, *ApJ*, 641, 556
- Mata Sánchez, D., González Hernández, J. I., Israelian, G., et al. 2014, *A&A*, 566, A83
- Mollière, P. & Mordasini, C. 2012, *A&A*, 547, A105
- Mordasini, C., Alibert, Y., Benz, W., Klahr, H., & Henning, T. 2012a, *A&A*, 541, A97
- Mordasini, C., Alibert, Y., Klahr, H., & Henning, T. 2012b, *A&A*, 547, A111
- Moutou, C., Vigan, A., Mesa, D., et al. 2017, *A&A*, 602, A87
- Naponiello, L., Bonomo, A. S., Mancini, L., et al. 2025, *A&A*, 693, A7
- Noyes, R. W., Hartmann, L. W., Baliunas, S. L., Duncan, D. K., & Vaughan, A. H. 1984, *ApJ*, 279, 763
- Osborn, A. & Bayliss, D. 2020, *MNRAS*, 491, 4481
- Panahi, A., Zucker, S., Clementini, G., et al. 2022, *A&A*, 663, A101
- Paxton, B., Marchant, P., Schwab, J., et al. 2015, *ApJS*, 220, 15
- Pinamonti, M., Barbato, D., Sozzetti, A., et al. 2023, *A&A*, 677, A122
- Ruggieri, A., Desidera, S., Sozzetti, A., et al. 2024, *A&A*, 689, A235
- Schneider, J. 2018, in *Handbook of Exoplanets*, ed. H. J. Deeg & J. A. Belmonte, 119
- Schwarz, G. 1978, *The Annals of Statistics*, 6, 461
- Skrutskie, M. F., Jones, T., Hinz, P., et al. 2010, in *Ground-based and Airborne Instrumentation for Astronomy III*, ed. I. S. McLean, S. K. Ramsay, & H. Takami, Vol. 7735, *International Society for Optics and Photonics (SPIE)*, 77353H
- Snedden, C. 1973, *ApJ*, 184, 839
- Soummer, R., Pueyo, L., & Larkin, J. 2012, *ApJ*, 755, L28
- Sozzetti, A. 2023, *A&A*, 670, L17
- Sozzetti, A., Damasso, M., Fernández Fernández, J., et al. 2024, *MNRAS*, 535, 531
- Sozzetti, A., Pinamonti, M., Damasso, M., et al. 2023, *A&A*, 677, L15
- Stefánsson, G., Mahadevan, S., Winn, J. N., et al. 2025, *AJ*, 169, 107
- Stevenson, A. T., Haswell, C. A., Barnes, J. R., & Barstow, J. K. 2023, *MNRAS*, 526, 5155
- Ter Braak, C. J. F. 2006, *Statistics and Computing*, 16, 239
- van Leeuwen, F. 2007, *A&A*, 474, 653
- Winn, J. N., Petigura, E. A., Morton, T. D., et al. 2017, *AJ*, 154, 270
- Zechmeister, M. & Kürster, M. 2009, *A&A*, 496, 577

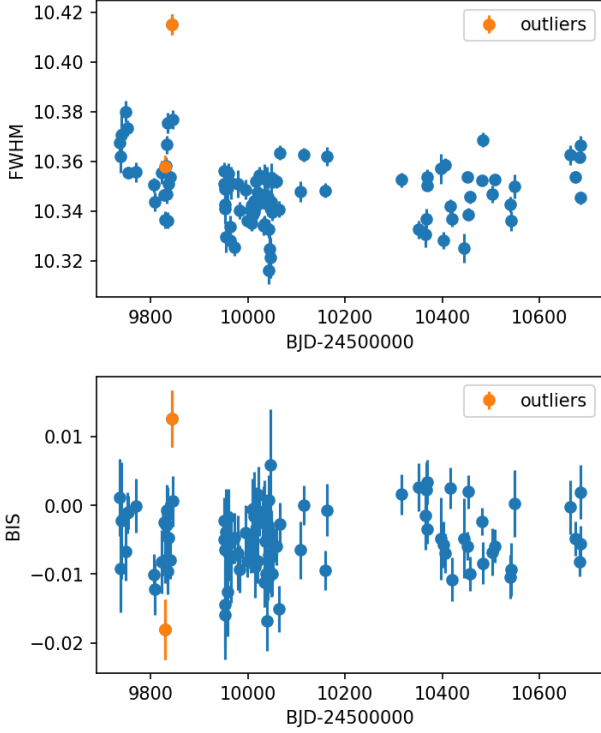


Fig. A.1: Time series of the HARPS-N CCF activity indicators. *Upper panel*: FWHM; *Lower panel*: BIS. The orange dots represents the outliers discussed in Sect. 4.2.

## Appendix A: Additional activity analysis

In addition to the  $\log R'_{\text{HK}}$  analysis, we studied two other activity indicators, derived from the CCF of the HARPS-N spectra via version 3.0.1 of the HARPS-N Data Reduction Software (DRS, Dumusque et al. 2021): the full width half maximum (FWHM) and bisector span (BIS). The two time series are shown in Fig. A.1. Of the two outliers discussed in Sect. 4.2, one can be clear seen as an outlier in both CCF activity time series.

Fig. A.2 shows the GLS periodograms of the two time series. The FWHM shows a significant peak at  $P = 422 \pm 27$  d, close to the one highlighted in the  $\log R'_{\text{HK}}$  time series (see Fig. 3), while the BIS does not show any significant periodicity above the FAP= 10% level.

## Appendix B: Gaia DR3 priors model

As an additional test to attempt reconciling the results from Gaia astrometry and HARPS-N RVs, we performed an MCMC fit of the RV time series using Gaussian priors from the Gaia orbital solutions, using the best-fit values and their uncertainties. The adopted values of these priors are listed in Table B.1. It is worth noticing that, while some parameters come directly from the orbital solutions published in the Gaia archive, such as those on  $P_b$  and  $T_{p,b}$ , the others were derived from the related parameters and corresponding uncertainties (see Sect. 2). One particular case is that of the semi-amplitude  $K_b$ , which directly depends on the companion mass, for which no uncertainty was provided in the Gaia DR3 catalogue: for this reason, we did not fix a Gaussian prior on  $K_b$  and adopted the uninformative prior from Table 3. The results of this fit are listed in the last columns of Table B.1: there is no significant deviation from the results of the original 1-Keplerian fit with uninformative priors from Table 3. This sug-

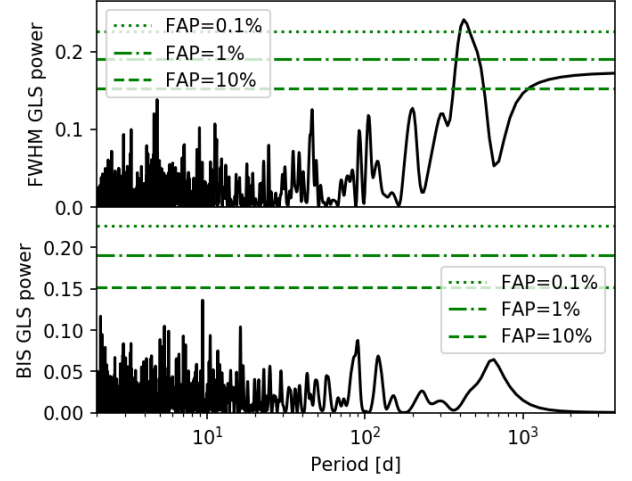


Fig. A.2: GLS periodograms of the HARPS-N CCF activity indicators. *Upper panel*: FWHM; *Lower panel*: BIS.

Table B.1: Priors and best-fit parameters for the tested Gaia-constrained MCMC model.

	Priors	Values
$K_b$ [m s <sup>-1</sup> ]	$\mathcal{U}(0,1000)$	$322.2^{+3.7}_{-3.5}$
$P_b$ [d]	$\mathcal{N}(1090, 310)$	$2513^{+72}_{-69}$
$T_{p,b}$ [BJD-2450000]	$\mathcal{N}(10490, 290)$	$10159.07^{+0.58}_{-0.60}$
$\sqrt{e_b} \cos \omega_b$	$\mathcal{N}(0.28, 0.32)$	$-0.229^{+0.011}_{-0.011}$
$\sqrt{e_b} \sin \omega_b$	$\mathcal{N}(-0.22, 0.41)$	$-0.8646^{+0.0048}_{-0.0048}$
$M_b \sin i$ [ $M_J$ ]		$14.70^{+0.50}_{-0.51}$
$a_b$ [AU]		$3.860^{+0.099}_{-0.097}$
$e_b$		$0.8002^{+0.0063}_{-0.0065}$
$\omega_{\star,b}$ [rad]		$-1.830^{+0.013}_{-0.013}$
$\gamma_{\text{HARPS-N}}$ [m s <sup>-1</sup> ]	$\mathcal{U}(-50.0, 250.0)$	$237.49^{+0.96}_{-0.95}$
$\sigma_{\text{jit,HARPS-N}}$ [m s <sup>-1</sup> ]	$\mathcal{U}(0,100)$	$5.25^{+0.44}_{-0.39}$

gests that the evidence from the RV time series is stronger than the constraint from the astrometric orbital solution, as expected.

## Appendix C: Stellar age and rotation period

As discussed in Sect. 3, the isochrones estimate of the stellar age points towards an intermediate age, although with large uncertainties,  $t_{\text{iso}} = 1.9^{+1.9}_{-1.3}$  Gyr. We consider here additional age diagnostics to further constrain the system age.

In Sect. 3, we highlighted the presence of a significant Lithium line in the spectra of HD 128717. The abundance of Lithium is commonly associated with a young stellar age, as Lithium depletes over time in main-sequence stars. However, comparing HD 128717 Lithium equivalent width and abundance, and its effective temperature with those of clusters of known age, the parameters of HD 128717 are in good agreement with the distribution of the open cluster NGC 752, which has a measured age of 1.34 Gyr (Agüeros et al. 2018).

Another common proxy for stellar age is the activity level: the mean  $\log R'_{\text{HK}} = -4.947$  is quite low. Following activity-rotation and gyrochronology relations (Noyes et al. 1984; Ma-



majek & Hillenbrand 2008), we can derive a rotation period of  $P_{\text{rot}} = 21 \pm 4$  d and an age of  $t = 3.7 \pm 0.4$  Gyr. However, this rotation period is incompatible with the measured projected rotational velocity,  $v \sin i = 6.1 \pm 0.5$  km s<sup>-1</sup> (in good agreement with the  $v \sin i$  relation by Winn et al. (2017)), that combined with the stellar radius  $R_{\star} = 1.248 \pm 0.024 R_{\odot}$  results in a maximum rotation period of  $P_{\text{rot, max}} = 10.3 \pm 0.9$  d.

In order to obtain a more precise estimate of the rotation period, we analysed 4 available TESS sectors (14,15,49 and 50) with the Python wrapper *juliet*<sup>9</sup> (Espinoza et al. 2019) using a quasi-periodic Gaussian process (GP) kernel implemented with *celerite* (Foreman-Mackey et al. 2017). The GP modelling converges on a period of  $3.9 \pm 0.3$  d.

If we interpreted this as the stellar rotation period, it would point towards a young age ( $\simeq 300$  Myr), in contrast with the other indicators. However, the peak in the GP posterior could correspond to the first harmonic of the stellar rotation, resulting in  $P_{\text{rot}} = 7.8 \pm 0.6$  d, which would correspond in a more compatible estimate of gyrochronological age,  $t_{\text{gyro}} = 900$  Myr.

Finally, we can obtain another estimate of the age of the system from its kinematic. We can compute the Galactic space velocity components  $U$ ,  $V$ , and  $W$  from the proper motion, parallax, and radial velocity of the system. We can get the Gaia DR3 parallax from Table 2 and, from the HARPS-N spectra collected, we can derive the absolute systemic velocity of the star using version 3.0.1 of the HARPS-N Data Reduction Software (DRS, Dumusque et al. 2021):  $\gamma_{\text{syst}} = +5.90776 \pm 0.00101$  km s<sup>-1</sup>. We do not use the Gaia DR3 proper motion components, as the measurements can be biased by the incorrect modelling of the Keplerian motion. For this reason, we adopt the proper motion from Brandt (2021), which is computed from the difference in position between the Gaia DR3 and Hipparcos catalogues, and therefore should not be affected by the orbital motion<sup>10</sup>:  $\mu_{\text{ra}} = -81.992 \pm 0.021$  mas yr<sup>-1</sup>,  $\mu_{\text{dec}} = +67.612 \pm 0.023$  mas yr<sup>-1</sup>. From these values, following the methodology by Johnson & Soderblom (1987), we obtain:  $U = -35.876 \pm 0.059$  km s<sup>-1</sup>,  $V = -10.698 \pm 0.013$  km s<sup>-1</sup>,  $W = -3.673 \pm 0.005$  km s<sup>-1</sup>. From these Galactic space velocities, we can compute the kinematical age of the system, as defined by Almeida-Fernandes & Rocha-Pinto (2018), as  $t_{\text{kin}} \simeq 1.4$  Gyr. It is worth mentioning that the kinematical age gives only an approximate estimate for single systems, and it is more informative for statistical samples, and in fact Almeida-Fernandes & Rocha-Pinto (2018) suggest an uncertainty of around 3 Gyr for individual stars. However, it is noteworthy that this value is in good agreement with the previous estimates.

Combining all these estimates, we can adopt the average value of the age for HD 128717  $t = 1.4 \pm 0.3$  Gyr.

## Appendix D: Direct imaging observations and analysis

In both observation epochs SHARK-NIR used its board-band H filter and Gaussian coronagraph with an inner working angle (IWA) of 120 mas, while LMIRCam observations were performed in the L' band using the vector-apodizing phase plate coronagraph (vAPP, Doelman et al. 2021) having an IWA of

246 mas. The coronagraphs IWAs correspond for HD 128717 to orbital separations of  $\sim 8$  and  $\sim 18$  au, meaning that HD 128717 B would remain covered by the central occulter even at apoastron and therefore undetectable. The April observations lasted  $\sim 40$  minutes and were characterized by rapidly variable seeing between  $1.09''$  and  $2.30''$ , while the May epoch lasted  $\sim 1$  hour with seeing between  $0.90''$  and  $1.49''$ .

The SHARK-NIR and LMIRCam data thus collected were reduced using a post-processing procedure based on the angular differential imaging method (ADI, Marois et al. 2006) method and the principal components analysis (PCA Soummer et al. 2012) algorithm. For both instruments, contrast limits were computed by estimating the standard deviation within one-pixel-wide annuli centred on the star, with the resulting contrast curves shown in the upper panel of Fig. 16.

## Appendix E: BD and GP statistical sample

To compare Gaia-6 B with the known population of BDs and GPs, we collected from the public archives a large sample of well characterized systems with BD and GP companions. First we selected from the NASA Exoplanet Archive<sup>11</sup> all objects with mass (or  $m \sin i$ )  $> 0.1 M_{\text{J}}$  and period  $< 10^4$  d, considering only the default solutions from the archive. Then we selected only the systems with a measured stellar mass and metallicity, resulting in 1138 companions. We then selected from the Encyclopaedia of Exoplanetary Systems<sup>12</sup> all brown dwarfs with mass (or  $m \sin i$ )  $> 13 M_{\text{J}}$ , selecting again only companions with period  $< 10^4$  d and measured mass and metallicity of the stellar host, corresponding to 78 companions. We then merged this sample with the catalogue of brown dwarf companions from Gaia DR3 selected by Stevenson et al. (2023) which, after applying the same selection as for the other two catalogues, contains 117 objects. Merging this three samples together, discarding duplicates, we obtain a sample of 1311 companions, with 1118 and 193 giant planets and brown dwarfs, respectively. Fig. 14 shows the distribution of companion mass as a function of the stellar mass and metallicity, while Fig. E.1 shows the period-eccentricity distribution of GPs and BDs. In both figures are highlighted Gaia-4,-5, and -6 B as well as HIP66074 b.

## Appendix F: emcee auxiliary plots

Fig. F.1 shows the complete posteriors of the 1-Keplerian model of the HARPS-N RV data, which was adopted as the best RV model.

<sup>9</sup> <https://juliet.readthedocs.io/en/latest/>

<sup>10</sup> The Gaia DR3 - Hipparcos proper motion could still be affected by additional undetected companions: although massive long-period companions undetected by the direct imaging observations (Fig. 16) could still produce significant astrometric distortion, this would not significantly affect the estimate of the kinematical age of the system.

<sup>11</sup> <https://exoplanetarchive.ipac.caltech.edu/>

<sup>12</sup> <https://exoplanet.eu/>

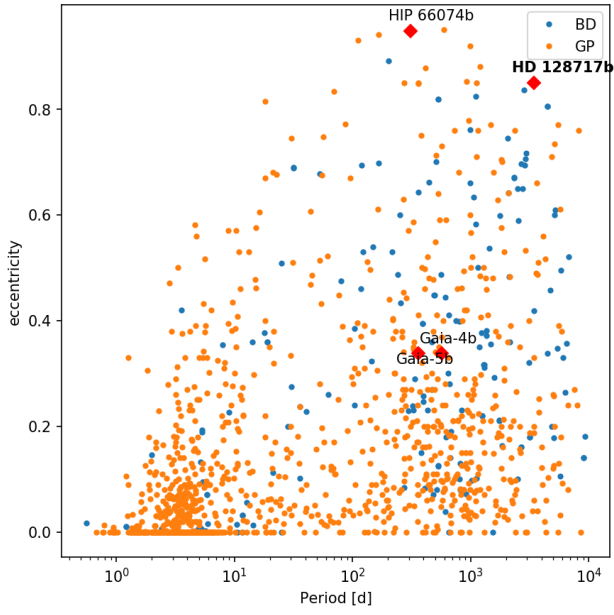


Fig. E.1: Eccentricity of giant planets (orange) and brown dwarfs (blue) as a function of the orbital period, for substellar companions with period  $< 10^4$  d. The red diamonds highlight the positions of the confirmed Gaia-ASOI sub-stellar companions and HIP 66074.

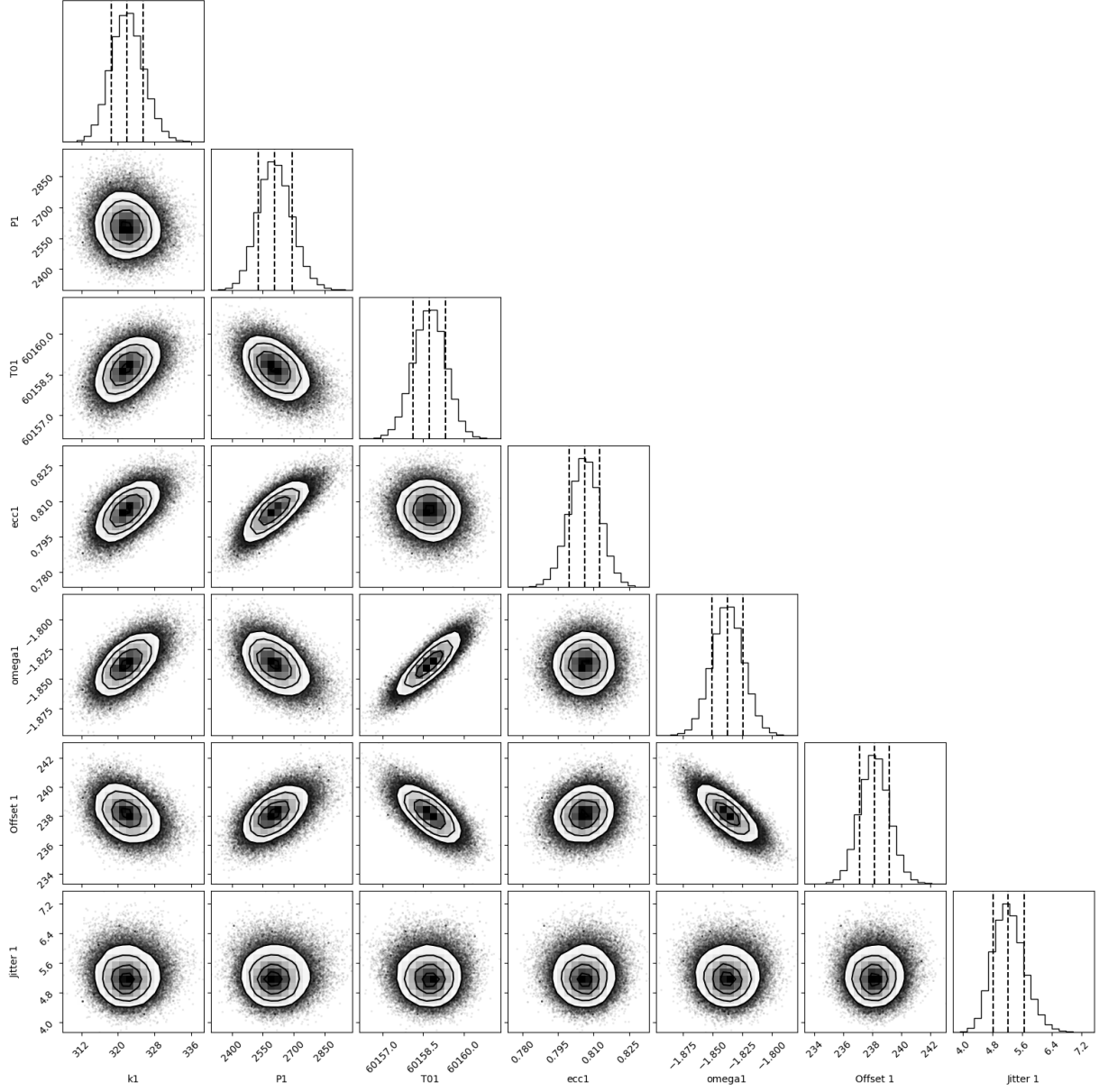


Fig. F.1: Posterior distributions of the fitted parameters of the 1-Keplerian model of the HARPS-N RV time series. The vertical dashed lines denote the median and the 16th and 84th percentiles. The shown parameters are, in order:  $k_b$ ,  $P_b$ ,  $T_{p,b}$ ,  $e_b$ ,  $\omega_b$ ,  $\gamma_{\text{HARPS-N}}$ , and  $\sigma_{\text{jitter,HARPS-N}}$